LANGMUIR

pubs.acs.org/Langmuir Article

Aspartic Acid Binding on Hydroxyapatite Nanoparticles with Varying Morphologies Investigated by Solid-State NMR Spectroscopy and Molecular Dynamics Simulation

Yuan Li, Christian D. Lorenz, and Gregory P. Holland*



Cite This: Langmuir 2024, 40, 22824-22834



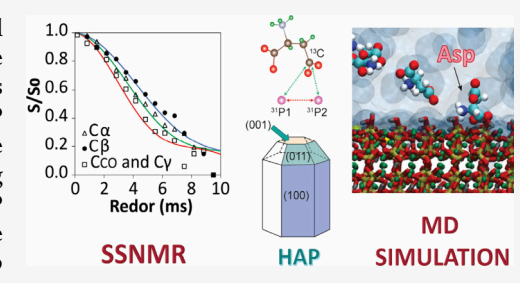
ACCESS I

Metrics & More

Article Recommendations

Supporting Information

ABSTRACT: Hydroxyapatite (HAP) exhibits a highly oriented hierarchical structure in biological hard tissues. The formation and selective crystalline orientation of HAP is a process that involves functional biomineralization proteins abundant in acidic residues. To obtain insights into the process of HAP mineralization and acidic residue binding, synthesized HAP with specific lattice planes including (001), (100), and (011) are structurally characterized following the adsorption of aspartic acid (Asp). The adsorption affinity of Asp on HAP surfaces is evaluated quantitatively and demonstrates a high dependency on the HAP morphological form. Among the synthesized HAP nanoparticles (NPs), Asp exhibits the strongest adsorption affinity to short HAP nanorods, which are



composed of (100) and (011) lattice planes, followed by nanosheets with a preferential expression of the (001) facet, to which Asp displays a similar but slightly lower binding affinity. HAP nanowires, with the (100) lattice plane preferentially developed, show significantly lower affinity to Asp and evidence of multilayer adsorption compared to the previous two types of HAP NPs. A combination of solid-state NMR (SSNMR) techniques including ¹³C and ¹⁵N CP-MAS, relaxation measurements and ¹³C-³¹P Rotational Echo DOuble Resonance (REDOR) is utilized to characterize the molecular structure and dynamics of Asp-HAP bionano interfaces with ¹³C- and ¹⁵N-enriched Asp. REDOR is used to determine ¹³C-³¹P internuclear distances, providing insight into the Asp binding geometry where stronger ¹³C-³¹P dipolar couplings correlate with binding affinity determined from Langmuir isotherms. The carboxyl sites are identified as the primary binding groups, facilitated by their interaction with surface calcium sites. The Asp chelation conformations revealed by SSNMR are further refined with molecular dynamics (MD) simulation where specific models strongly agree between the SSNMR and MD models for the various surfaces.

1. INTRODUCTION

Hydroxyapatite (HAP) is the predominant inorganic constituent of biological hard tissue such as bone and teeth. ^{1–3} It presents in different forms and crystal phases at different stages of its deposition during biomineralization, which is a process regulated by functional and structural proteins. ^{4–8} The bioactivity of HAP is associated with its morphology, crystallinity, and the terminating groups from different lattice planes. The (100) and (001) lattice planes of HAP are the most studied facets due to the important roles they play in the process of biomineralization. The (100) plane is the predominant lattice plane that grows parallel to triple helical collagen along the axial direction, and the (001) plane is formed in the hole-zone between the collagen, contacting N and C terminal groups and is expressed at a much lower ratio compared to (100) in bioapatite. ^{9–15}

Numerous efforts have been made to elucidate the chemical structures of these surfaces with both computational and experimental approaches. The simulated structural models of each lattice plane are derived by cutting slabs along certain crystal orientations followed by relaxation under different physicochemical environments (i.e., water solvation) for

optimized geometries. ^{16,17} The (100) and (001) planes with minimized energy are generally recognized as surfaces that are positively charged by Ca²⁺ and rich in PO₄³⁻ with negative charges, respectively. ^{1,16,18} However, the ratio of these sites on HAP surfaces can be influenced by the physiological or synthetic (surfactant and pH) conditions during the formation of HAP. ^{19–24} The synthesized surfaces with preferred lattice parameters do not perfectly agree with the computational results due to these chemical modifications. For example, some surface charge measurements showed that the actual (100) lattice plane carries negative charge and is terminated with O atoms from phosphate groups in water at a pH of 7. ^{25,26}

In our previous work, HAP nanoparticles (NPs) with different morphologies and crystallographic orientations, including nanowires (aHAP) with the (100) lattice plane

Received: July 26, 2024
Revised: October 3, 2024
Accepted: October 10, 2024
Published: October 21, 2024





preferentially developed (Figure 1a), nanosheets (cHAP) with the (001) facet highly expressed (Figure 1b) and nanorods

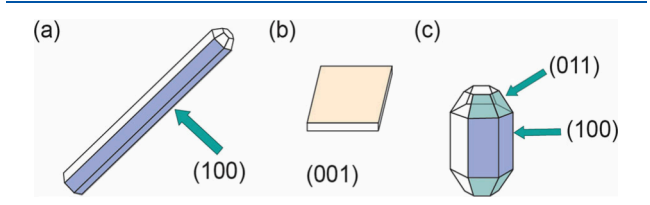


Figure 1. Illustration of synthesized HAP NPs including (a) nanowires, (b) nanosheets and (c) nanorods.

(rHAP), a polycrystalline HAP that exhibit hybrid lattices including (100) and (011) (Figure 1c) were synthesized and examined with $^{31}\mathrm{P}$ and $^{1}\mathrm{H}$ MAS solid-state nuclear magnetic resonance (SSNMR). 27 L-Aspartic (Asp) acid and L-arginine (Arg) were adsorbed on these surfaces to probe the chemical environment by displacing the surface bound groups including water molecules, hydroxyl groups and protons. In this study, it was found that the aHAP appeared to be a $\mathrm{PO_4}^{3-}$ rich surface whereas cHAP displayed a significant amount of exposed surface hydroxylated calcium defects, which could be attributed to the addition of ethylenediaminetetraacetic acid (EDTA) in the synthesis, which is a strong calcium chelating reagent. 27

In order to obtain further insights into the interface between biomolecules and different HAP lattice planes, we continued this work from the perspective of adsorbates by observing the molecular details of adsorbed Asp with SSNMR spectroscopy together with molecular dynamics (MD) simulations. Poly carboxylate compounds, like citrate, and domains containing acidic residues (Asp and Glu) in biomineralization proteins are known to play a significant role in controlling the process of HAP mineralization. 15,28-31 For example, citrate is found in bone where it serves as an inhibitor for the growth of HAP nanocrystals by stabilizing the mineral interface. 32,33 Asp, with its negatively charged carboxyl groups, exhibits a strong affinity for calcium ions and is periodically encoded in human type I collagen, rendering it an important HAP nucleator. 14,34 Additionally, as a representative amino acid enriched in the noncollagenic proteins (NCP) present in dentin, Asp is believed to induce the nucleation of HAP in teeth. 35,36 Given the important role Asp plays in the process of biomineralization and its strong affinity for HAP surfaces,²² it has been selected as the binding ligand to probe the surface chemistry of the synthesized HAP NPs in the present study.

SSNMR has been widely applied in studies aimed at elucidating the binding interface between peptides and HAP surfaces. The Actational Echo DOuble Resonance (REDOR) SSNMR techniques are commonly used to estimate the distances between the surface TP and TS C or TS From the adsorbate molecules up to 8 Å. The strength of the dipolar interaction is inversely proportional to the third cube of the internuclear distance, which is measured by the rate of signal dephasing at various echo periods. This technique has been proven to be particularly valuable in identifying the binding configuration of biomolecules on HAP surfaces. In this study, the Asp binding on synthesized, morphologically distinct HAP NPs is characterized with this method, together with 1D TC and TS CP-MAS and relaxation measurements for an in depth atomic-level understanding of the Asp-HAP bionano interface structure and dynamics. MD simulations are

incorporated to provide structural models of adsorbed Asp on each type of HAP surface to further refine our understanding of the conformation and organization of Asp bound on these morphologically distinct HAP NPs. The end goal is to elucidate the role of HAP morphology on Asp structural binding.

2. EXPERIMENTAL SECTION

2.1. Material. The three types of HAP nanoparticles with different morphologies analyzed in this study include nanocrystalline short rods (rHAP), long nanowires (aHAP) and nanosheets (cHAP) that were synthesized following synthetic methods reported previously. Fully labeled U-[15 N/ 13 C]-L-aspartic acid (98%) was purchased from Cambridge Isotopes Inc. L-aspartic acid (C₄H₇NO₄, 98%) was obtained from Acros. Sucrose (C₁₂H₂₂O₁₁, 99.5%) and O-phospho-L-serine (OPLS) (C₃H₈NO₆P, 99%) were purchased from Sigma-Aldrich. Phenyl isothiocyanate (PITC) (C₆H₅NCS, 99.0%) was purchased from Thermo Scientific. Acetonitrile (ACN, CH₃CN, 98%) was obtained from Fisher Scientific.

2.2. Adsorption Isotherm. Asp stock solution (100 mM) with pH adjusted to 7.5 by NaOH was prepared and diluted to various concentrations for standard curves and adsorption sample preparation. About 15 mg (± 0.25 mg) of HAP nanoparticles were accurately weighed and added to 2 mL microcentrifuge tubes. Ultrapure water (0.5 mL) was added to the solids and sonicated at room temperature for 45 min to break the large agglomerates. Asp solutions (0.5 mL) were added to each sample to make the initial Asp concentration that varied from 0.5 to 50 mM and the mixtures were stirred at 300 rpm at 25 °C for 24 h. The liquid and solid phases were separated by centrifugation at 10000 rpm for 45 min. The supernatant of each sample was isolated for quantitative analysis.

The Asp adsorption loadings onto different HAP surfaces were evaluated quantitatively by comparing the differences between the concentrations of Asp solutions before and after adsorption. 22,43,44 Asp was derivatized with PITC for an optimized UV absorbance at 254 nm following the procedure reported by Zheng et al. 45 Calibration curves over a concentration range from 0.25 to 15 mM were obtained after the precolumn derivation. Aliquots of Asp solution at volumes from 20–100 μ L were sampled from the supernatant and diluted to concentrations ranges from 4–10 mM to ensure the data points fall in the middle of the calibration curves. All the samples were analyzed with high-performance liquid chromatography (HPLC) using an Agilent 1100 HPLC system equipped with an Agilent Zorbax Extend C18 column (2.1 mm \times 50 mm \times 3.5 μ m) at 23 °C.

The adsorption complexes (Asp-HAP) for SSNMR analysis were prepared with fully labeled U-[$^{15}\mathrm{N}/^{13}\mathrm{C}$]-L-Asp at an initial concentration of 50 mM following the same procedure as discussed above. The solid sediments were dried under vacuum at room temperature for 48 h for SSNMR analysis to minimize adsorbed water.

2.3. Brunauer–Emmett–Teller (BET) Surface Area of HAP NP. The Brunauer–Emmett–Teller (BET) surface areas of aHAP and cHAP NP were analyzed with an Anton Paar Quantachrome autosorb IQ automated gas sorption analyzer. HAP NP powders (0.1–0.3 g) were outgassed at 80 $^{\circ}$ C for 1 h. The nitrogen adsorption isotherms at 77.35 K were measured. The BET surface area of rHAP was calculated based on the nitrogen adsorption–desorption isotherm at –196 $^{\circ}$ C collected with a Micrometrics ASAP2020 porosimeter as reported previously.²⁷

2.4. Amino Acids Standard Preparation. The fully protonated crystalline Asp was analyzed as received. The Asp in an amorphous phase was prepared by dissolving Asp (0.03 M) and sucrose at a molar ratio of \sim 1:3. Sucrose was added to inhibit the amino acids from crystallization during the dehydration step. ⁴⁶ The pH of the solution was adjusted to \sim 7 with NaOH to keep the amino acid molecules in a fully charged state. The mixture was freeze-dried in a Labconco Freezone lyophilizer at -89 °C under vacuum pressure of 0.06 Mbar for 36 h.

2.5. Solid-State Nuclear Magnetic Resonance. The structures of adsorbed Asp on HAP surfaces were characterized by SSNMR. The samples were filled into zirconia magic angle spinning (MAS) rotors immediately following removal from the vacuum desiccator, to minimize the influence of water molecules from the atmosphere.

All the ¹³C and ³¹P experiments were collected with a 3.2 mm ¹H/³¹P/¹³C BioSolids MAS probe in a 600 MHz Bruker AVIII Spectrometer. The resonance frequencies of ¹H, ¹³C and ³¹P were 598.9 MHz, 150.6 and 242.4 MHz. $^{1}H \rightarrow ^{13}C$ CP spectra were collected at a MAS frequency of 12 kHz. The experiment started with a $\pi/2$ pulse having a duration of 2.5 μ s on the ¹H channel, followed by a Hartmann-Hahn match condition achieved by square pulse on ¹H channel at 65 kHz and 30% ramped pulse on the 13 C channel at +1 ν_{R} RF field strength for a contact time duration of 2 ms. 47,48 ¹H-¹³C heteronuclear dipolar decoupling was achieved by swept-frequency two-pulse phase modulation (swfTPPM) pulse scheme at a RF field of 100 kHz on the ¹H channel. ^{49,50} A total of 1024 number of scans (NS) were collected with a recycle delay of 3.0 s for each ¹³C CP-MAS NMR spectrum. The 13C chemical shift was indirectly referenced to TMS by setting the CH peak of adamantane to 38.4 ppm.5

The longitudinal (T_1) relaxation of 1H and ^{13}C from surface bound Asp molecules was determined via inversion recovery with CP detection. $^{52-56}$ The ^{13}C T_1 spectra were collected with the CP enhanced inversion recovery introduced by Torchia, with relaxed signal detected after delays from 0.5 to 30 s. 52,57 The 1H T_1 relaxation times were obtained with inversion recovery $(\pi - \tau - \pi/2)$ after delay times (τ) from 0.01 to 5 s. 56,57 The relaxed signal was detected through a $^1H \rightarrow ^{13}C$ CP transfer as ^{13}C signal. Four hundred NS were collected for each delay time for both ^{13}C and 1H T_1 experiments.

 $^{1}\text{H} \rightarrow ^{15}\text{N}$ CP-MAS spectra were collected with a 1.9 mm $^{1}\text{H}/^{13}\text{C}/^{15}\text{N}$ MAS probe at 30 kHz MAS rate. The resonance frequencies of ^{1}H and ^{15}N were 598.9 and 60.7 MHz. The CP condition for this experiment comprised of a 2.4 μs ^{1}H $\pi/2$ pulse and a 1.5 ms 30% ramped ^{1}H spin-lock pulse with a RF field of 100 kHz. $^{1}\text{H}-^{15}\text{N}$ dipolar couplings were removed with swfTPPM at an RF field of 117 kHz on the ^{1}H channel. A total of 1024 NS were averaged with a recycle delay of 5 s. The chemical shift of ^{15}N is referenced to MLF. 58,59

³¹P-dephased, ¹³C-detected REDOR experiments were carried out using the pulse sequence shown in Figure 2. A ¹³C transverse

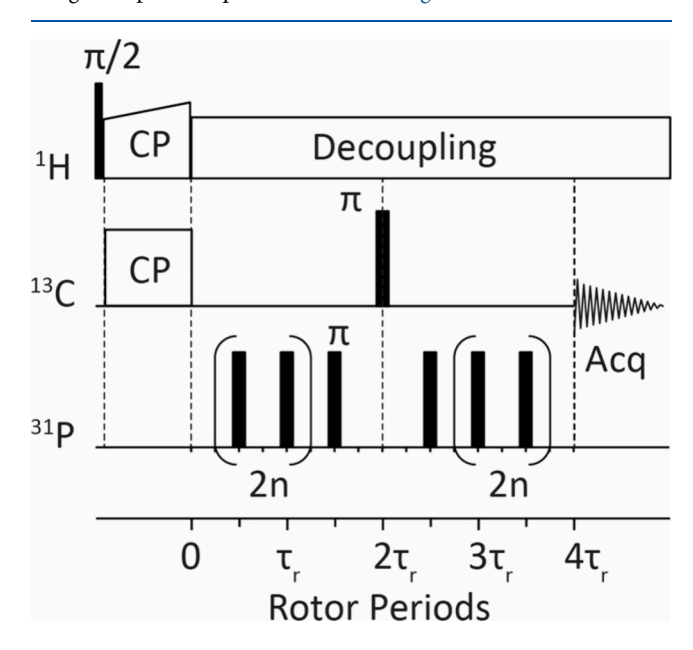


Figure 2. ³¹P-dephased, ¹³C-detected REDOR pulse sequence enhanced by $^1H \rightarrow ^{13}C$ CP. Two π pulses were applied in each rotor period (τ_t) .

magnetization was initiated by $^1H\to ^{13}C$ CP at an RF field of 65 kHz. Rotor synchronized π pulse trains (RF at 50 kHz) with a XY-8 phase cycling scheme were applied on the ^{31}P channel. One refocusing ^{13}C π pulse of 6 μs placed in the middle of the spin revolution period is included to refocus the ^{13}C chemical shift evolution. A spectrum was collected with no ^{31}P π pulse train applied immediately after each dephased spectrum with the same delay period as a reference during which T_2 type signal losses were recorded. $^{60-62}$

The experimental REDOR curves were compared to numerically simulated dephasing curves in SIMPSON that were determined with various 13C-31P dipolar interactions.63 The simulations were conducted with a set of 320 Euler angles with the REPULSION method and 18 γ equally spaced angles.⁶⁴ Ideal RF pulses that are infinitely short and strong with frequencies that match the experimental values were used in these simulations. 63 Spin systems that contain one carbon atom from Asp and two adjacent phosphorus atoms on HAP surfaces were created for the simulations following the method reported by Drobny et al.³⁷ The isotropic chemical shift $(\delta_{\rm iso})$, chemical shift anisotropy (CSA) and asymmetry parameter (η) of ³¹P were determined to be 2.9 ppm, 13.4 ppm and 0.75 by line fitting to the ³¹P CP-MAS NMR spectrum of aHAP collected at a MAS rate of 5 kHz with ssNake (Figure S1).⁶⁵ The chemical shielding tensor parameters of ¹³C spins were obtained from previously reported studies. ^{66,67} Crystallized OPLS was prepared and analyzed as a model compound to set up the REDOR experiment and validate the simulations following the method reported by Greenwood et al. as described in the Supporting Information. 41 The REDOR experimental and simulated results of OPLS are provided in Figure S2 and Table

2.6. Molecular Dynamics Simulations of Interface between Asp and HAP. We generated initial structures of the hydrated slabs of three different crystalline forms of HAP at two different pHs using the Nanomaterial Modeler within CHARMM-GUI (Table S2).^{68,} We then equilibrated the HAP with the aqueous environment which contained 200 mM NaCl following the simulation protocol prescribed by CHARMM-GUI: (i) steepest decent minimization, (ii) molecular dynamics simulation with the constant number, volume and temperature (NVT) ensemble employing the Nose-Hoover thermostat to control the temperature around a target temperature of 300 K and a 1 fs time step for 125 ps and (iii) a final molecular dynamics simulation with the constant number, pressure and temperature (NPT) ensemble employing the Nose-Hoover thermostat and the Parrinello-Rahman barostat to control the temperature and pressure around targets of 300 K and 1 bar, respectively. This final MD simulation was run for 100 ns.

After equilibrating these different hydrated HAP systems, we then randomly inserted 20 aspartic acid molecules into the aqueous phase of the systems. We then re-equilibrated these systems utilizing the following simulation protocol: (i) steepest decent minimization, (ii) a MD simulation with the NVT ensemble employing the Berendsen thermostat ($T=300~\rm K$) and 1 fs time step for 250 ps, (iii) a MD simulation with the NPT ensemble employing the Berendsen thermostat ($T=300~\rm K$) and Berendsen barostat ($P=1~\rm bar$) and a 1 fs time step for 125 ps, (iv) a MD simulation with the NPT ensemble employing the Berendsen thermostat ($T=300~\rm K$) and Berendsen barostat ($P=1~\rm bar$) and a 2 fs time step for 1.5 ns and finally (v) a production MD simulation with the NPT ensemble employing the Nose–Hoover thermostat ($T=300~\rm K$) and Parrinello–Rahman barostat ($P=1~\rm bar$) and a 2 fs time step for 100 ns.

The interactions of the HAP are described by the INTERFACE force field, ^{21,70} while the interactions of the water, ions and aspartic acid molecules are described by the CHARMM36m force field. ⁷¹ A short-range interaction cutoff of 1.2 nm was used in all simulations, and the PME algorithm was used to determine the long-range electrostatic interactions. The LINCS algorithm was used to constrain all hydrogen-containing bonds in order to allow us to utilize a 2 fs time step.

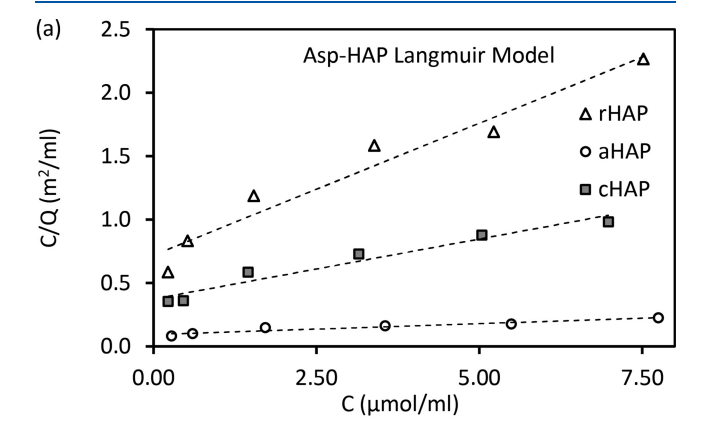
All of the analysis reported in this manuscript is done over the last 10 ns of the production simulations. The analysis was performed using scripts that have been written in house and built on top of the functionality of MDAnalysis. 72,73

3. RESULTS AND DISCUSSION

3.1. Adsorption Behavior of Amino Acids on HAP Surfaces. The affinity of Asp for different HAP surfaces was evaluated quantitatively and fitted to the Langmuir type adsorption model with linear regression using Excel (eq 1):⁷⁴

$$\frac{C}{Q} = \frac{1}{KN} + \frac{C}{N} \tag{1}$$

In this equation, C (μ mol/mL) is the Asp concentration when the adsorption reaches equilibrium and Q (μ mol/m²) is the amount adsorbed per unit surface area. The adsorption constants K (ml/ μ mol, affinity between the adsorbates and the surface) and N (μ mol/m², maximum adsorption capacity) were estimated by fitting C/Q and C to a linear relationship (Figure 3a). The adsorption isotherm curves were plotted



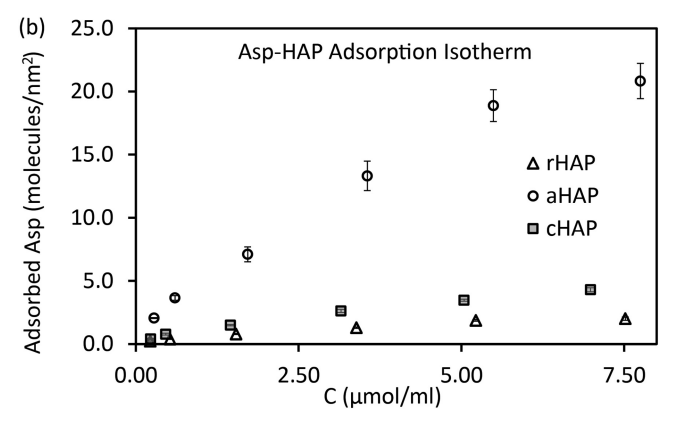


Figure 3. Adsorption isotherms of Asp on rHAP, aHAP and cHAP (a) fitted to Langmuir type model and (b) molecular coverage per unit surface area as a function of equilibrium concentrations.

with molecular surface coverage (molecule/nm²) vs C as displayed in Figure 3b. A full plot that has all the data points included can be found in Table S3 and Figure S3. The adsorption isotherms plotted with Q and C are presented in Figure S4 to provide a better visualization of the difference between the single layer and multilayer adsorption of Asp on various HAP samples. The experimental results and calculated results of surface coverage are summarized in Table 1.

Among three different types of HAP NPs, aHAP shows the highest capacity to adsorb Asp per unit surface area, as shown in Figure 3b. The affinity between Asp and the HAP surfaces

Table 1. BET Surface Area of HAP NPsa

	rHAP	aHAP	cHAP				
BET surface area (m²/g)	48.826	4.234	28.013				
amount of adsorbate for SSNMR samples $(\mu \text{mol/mg})$	0.38	0.46	0.82				
Langmuir Model							
$K \left(\text{ml}/\mu \text{mol} \right)$	0.29	0.18	0.25				
$N \left(\mu \text{mol/m}^2 \right)$	4.80	58.48	10.57				
R^2	0.9507	0.9231	0.9501				

"The loading of Asp per unit mass for each type of HAP for SSNMR analysis. Based on the adsorption of Asp at various initial concentrations onto synthesized HAP at 25 °C, the numbers of adsorption sites per unit surface area (N) and the affinity of the adsorbates to the adsorption sites (K) were fitted to the Langmuir adsorption model.

are reflected by the K coefficient, where higher K values indicate higher affinity between the adsorbate and the surface. rHAP surfaces show the strongest affinity for Asp, followed closely by cHAP while aHAP is found to have the weakest affinity. The calculated K coefficient generally agree with the data reported by the Hay group. 22,74

Since the length of Asp is 5.78 Å and the radius of the molecule is 3.32 Å with one terminal functional group anchored at HAP surface Ca,²² the maximum numbers of Asp molecules that 1 nm² can accommodate is about 3, without considering the actual numbers of binding sites on lattice facets. Therefore, only rHAP exhibited approximately a monolayer at the highest concentration since the numbers of Asp molecules per unit surface area are mostly below 3 as shown in Table S3. aHAP shows high surface coverage despite its low surface area, which strongly suggests a multilayer adsorption on the surface. The weaker Asp interactions with the aHAP surface could promote stronger interactions between Asp molecules resulting in multilayer adsorption. The results generally indicate that higher affinity correlates with higher surface area and multilayer deposition is observed for lower surface area samples.

3.2. Solid-State NMR of Asp-Hap. In order to determine molecular details of Asp binding on different types of HAP NPs, the dried Asp-HAP adsorption complexes were analyzed by ${}^{1}H \rightarrow {}^{13}C$ and ${}^{1}H \rightarrow {}^{15}N$ CP-MAS SSNMR. The Asp-HAP adsorption complexes were compared to crystalline and amorphous Asp in sucrose as displayed in Figure 4. At pH 7.5, Asp carries one net charge with its C_{CO} group and C_{γ} carboxyl group deprotonated, and the amine group protonated. C_{α} and C_{β} resonate at ~53 ppm and ~38 ppm in both crystalline and amorphous states. The amorphous form shows significant line broadening compared to the crystalline Asp. The C_{CO} and C_{γ} peaks are not distinguishable and show a merged broad peak at ~177.6 ppm for amorphous Asp, while for the crystalline sample, there are two resonances resolved at 176.6 and 175.3 ppm which can be assigned to C_{γ} and C_{CO} , respectively.

The adsorbed Asp shows broad peaks similar to the standard compound in amorphous form indicating a high degree of structural heterogeneity when adsorbed to HAP surfaces. Peak deconvolution with MestreNova revealed that the C_{α} signal from Asp bound to aHAP surfaces contains a center peak and two small shoulders, while for rHAP and cHAP, the C_{α} peaks only show one, broad component. C_{β} peaks display a main peak at ~37 ppm and a small shoulder at ~39 ppm for all the Asp-HAP samples. Notably, aHAP clearly shows an extra peak

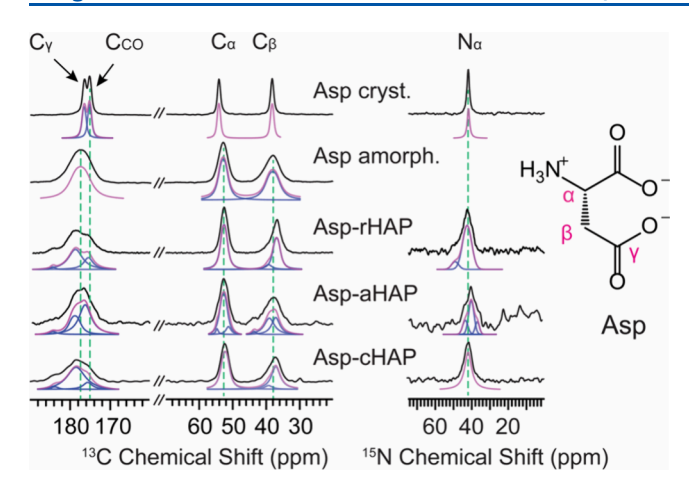


Figure 4. 13 C and 15 N CP-MAS SSNMR spectra (black) of Asp standards in crystalline and amorphous forms and adsorbed states on different types of HAP NP surfaces. Blue and red spectra represent the deconvoluted and sum of spectra simulations with MestreNova. The structure of Asp at pH = 7.5 is also shown.

at \sim 44 ppm in addition to these two peaks. Three broad components can be resolved at chemical shifts of 176, 178, and 182 ppm under the carboxyl region for all the Asp-HAP adsorption samples, suggesting these groups are involved in multiple binding environments. Similar observations have been reported by Goobes et al., demonstrating perturbed chemical shifts of carboxyl groups in osteonectin adsorbed on the surface of (100) HAP. The parameters from the peak fitting used are provided in Table S4.

The 15N CP-MAS NMR spectrum of the crystalline Asp standard shows a sharp peak with a full width at half-maximum (fwhm) ~ 96 Hz positioned at 40.8 ppm. A broad Asp peak is observed at similar chemical shift for cHAP (fwhm $\sim 281 \text{ Hz}$) and rHAP (fwhm ~ 367 Hz) adsorption complexes. For aHAP, a sharp peak (fwhm ~ 218 Hz) and two overlapped small peaks were observed. The detailed peak fitting parameters are presented in Table S4. The significant line broadening for all Asp adsorption samples indicates the NH₃⁺ moiety could potentially participate in surface binding. However, there was no clear chemical shift perturbation compared to the crystalline Asp. Overall, the combination of ¹³C and ¹⁵N CP-MAS NMR clearly indicates the carboxyl groups participate in binding, as these resonances are the broadest and multicomponent in the ¹³C CP-MAS NMR spectra and exhibit significant chemical shift perturbations compared to the crystalline and amorphous forms. Meanwhile, contributions from NH3+ binding cannot be discounted as evidenced by the significant line broadening observed in the ¹⁵N CP-MAS NMR spectra. It is noteworthy that although the loading of Asp on aHAP is only slightly higher than on rHAP, the CP-MAS spectra collected on Asp-aHAP exhibit a much lower signal-to-noise (S/N) ratio, particularly in the ¹⁵N CP-MAS spectra, compared to the other two types of Asp-HAP samples. The lower S/N for aHAP, in comparison to the other samples, is likely due to its significantly lower surface area over an order of magnitude less than rHAP (see Table 1). Based on 13 C and 1 H T_1 relaxation (Table S5), these S/N differences in CP-MAS spectra are not attributed to dynamic differences, as rHAP, which is the most dynamic, yields the best S/N. This supports the conclusion that the S/N

differences are due to variations in surface area among the samples, rather than dynamic differences.

³¹P-Dephased, ¹³C-Detected REDOR: Asp-HAP. ³¹P-dephased, ¹³C-detected REDOR curves for Asp on different types of HAP NP surfaces were collected to provide distance restraints regarding Asp binding geometries. The ¹³C-³¹P distances were estimated by comparing the experimental dephasing curves with numerical simulations conducted with SIMPSON.⁶³ The simulation was first conducted with a basic 2-spin system calculation to obtain approximate ¹³C-³¹P distances between a ³¹P spin from HAP surface phosphate to each ¹³C spin on Asp (Figure S5). Utilizing these estimated distances, two surface 31P atoms with an effective dipolar coupling of 600 Hz as determined previously³⁷ for HAP were then incorporated in the simulations as illustrated in Figure 5. The numerically simulated curves were optimized by varying the dipolar interaction between ¹³C and the additional ³¹P, and making fine adjustments on the primary ¹³C-³¹P spin pair. ⁷⁹

Asp bound to the surface of rHAP shows a binding pattern with C_{CO} and C_v to be the groups that locate closest to the surface at an estimated ¹³C-³¹P distance around 4.01 Å, followed by C_{α} and C_{β} at distances of 4.25 and 4.44 Å, respectively. The binding interaction of Asp bound to cHAP shows a similar trend but slightly longer distances compared to rHAP. rHAP is the surface with the closest binding distance to Asp, despite a lower adsorption capacity and higher degree of surface dynamics as indicated in the quantitative adsorption and NMR relaxation analysis (see the Supporting Information, Table S5), respectively. This adsorption behavior could be attributed to the (011) surface, which presents in relatively high amount in short nanorods. 27,80,81 The overall distances from the immobilized Asp to the surface of aHAP are observed to be longer by showing slower REDOR dephasing rates. C_{CO} and C_{γ} are the groups that are closest to the surface while C_{α} and C_{β} show similar but longer binding distances. This could indicate that the Asp is bound to aHAP with a bidentate bridging binding geometry by the chelation of C_{CO} and C_{ν} to surface calcium, or it could result from multilayer adsorption leading to longer ¹³C-³¹P distances and weaker dipolar couplings. In all Asp-HAP samples, REDOR measurements indicate that carboxyl groups are the closest to the HAP surface, with phosphate groups approximately 4 Å away. This finding is consistent with similar REDOR measurements for citrate adsorbed to bone, where citrate carboxyl groups were also found near phosphate groups at a similar distance.³³ Overall, the distances determined by REDOR, where shorter distances indicate stronger binding, agree with Langmuir binding affinity where rHAP > cHAP > aHAP.

3.3. MD Simulation. MD simulations were used to evaluate the expected atomic distances between C and N atoms from Asp and the P and Ca species on HAP surfaces and make comparisons with SSNMR results. The probabilities of these C–P distances at a range from 3 to 7 Å were estimated. The probability distributions of C–P distances are generated as presented in Figures S6–S11. Each distribution (A) was fitted to a Gaussian function to determine the mean distances (μ) and standard deviation (σ) (Tables S6–S11). Among all models, C_{α} –P distances are predicted to show consistent results with one major distribution at the distance of 4.46 \pm 0.09 Å, while C_{β} –P distances show multiple distributions at similar probability. Also, since it is difficult to discern the signals of C_{CO} and C_{γ} in the NMR analysis, these distances cannot be directly compared to the distances obtained from

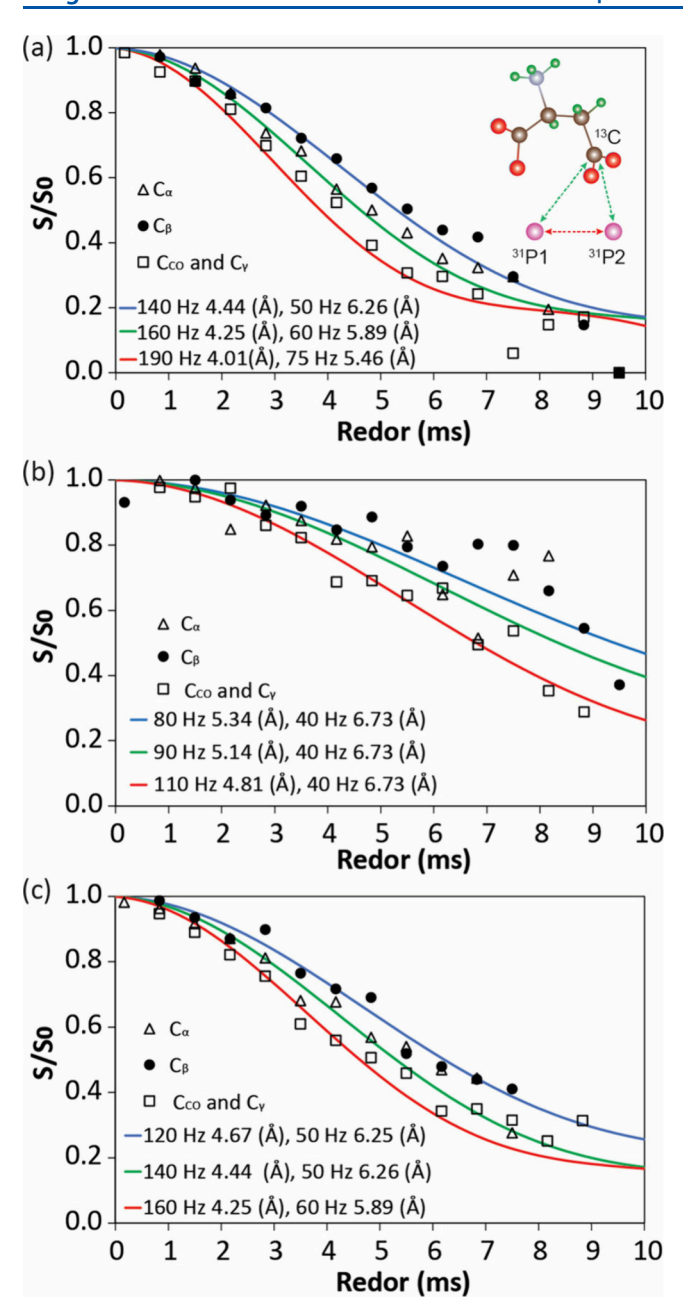


Figure 5. REDOR dephasing curves showing the relative peak area (S/S_0) as a function of dephasing time (τ) of Asp C_α (open triangles), C_β (filled circles) and C_{CO} and C_γ (open squares) adsorbed on (a) rHAP composed of (100) and (011) lattice planes, (b) aHAP and (c) cHAP, which are dominated by (100) and (001) planes, respectively. Experimental data are compared to dephasing curves calculated in SIMPSON (solid lines).

REDOR NMR. Therefore, the binding configurations of Asp on various HAP surfaces were generated based on the C_{β} -P distances with the highest probabilities for the potential binding models. Taking Asp on (001) lattice plane at pH 5 as an example, two binding configurations and the C-P distances for all other C atoms on Asp were estimated with C_{β} -P distances restrained at 4.33 and 5.03 Å (Figure S6 and Table S6).

The theoretical surface structures at pH 5 or 10 were obtained using the Nanomaterial Modeler within CHARMM-GUI. These models were then equilibrated in a 200 mM NaCl solution to have the surface groups relax and exchange water

molecules in this aqueous environment as described in the Experimental Section. Both the initial and equilibrated surface structures are provided in Figure S12. Due to the symmetry of the hexagonal crystal, the (100) plane is equivalent to the (010) plane, thus the surface model of (010) plane by MD was employed for the simulations conducted on the (100) plane. Similarly, (101) plane is adopted for the simulation of (011) plane in rHAP. These hydrated surfaces were then interfaced with Asp and equilibrated for the optimal binding structures. The C-P distances for each carbon atom in Asp and the surface phosphorus atoms in the different lattice planes of HAP are summarized in Table S12, and the corresponding Asp-HAP binding configurations are presented in Table S13. The bound structures representing the C-P distances from REDOR analysis are also presented in Tables S12 and S13.

Three representative models of Asp-HAP binding configurations by MD simulation were selected for each synthetic HAP NPs based on the dominant lattice planes and pH of the synthetic conditions. The selected models are (001) plane at pH 5, (010) plane at pH 5 and (101) plane at 10 for cHAP, aHAP and rHAP, respectively. These models are compared to experimental C–P distances estimated by REDOR as displayed in Table 2. The binding structures and the charts showing the distributions of probabilities of C_{β} –P from MD simulations are illustrated in Figure 6.

Table 2. Comparison of C and N Distances from Asp to P on HAP Lattice Planes from MD Simulation and REDOR for HAP NPs

Method	HAP Lattice Plane	C_{α} -P	С _β −Р	C _γ -P	C _{CO} -P	N-P
MD simulation (Å)	(001) pH 5	4.41	4.31	4.10	4.19	3.8
	(010) pH 5	4.40	5.40	4.13	4.41	3.5
	(101) pH 10	4.18	4.47	3.80	3.81	3.7
REDOR distance (Å)	cHAP	4.44	4.67	4.25 ^a		N/A
	aHAP	5.14	5.34	4.	81 ^a	N/A
	rHAP	4.25	4.44	4.	01 ^a	N/A

"Since the REDOR signal of C_{CO} and C_{γ} are not distinguishable, there is only one distance showing the average C-P distances between surface P and these two C atoms on carboxyl groups.

Since cHAP was synthesized in an acidic environment (initial pH \sim 4 to final pH \sim 6.5) with (001) plane being the predominant lattice plane, the Asp-HAP binding model at pH 5 is selected, as presented in Figure 6 (a). The initial (001) lattice plane at pH 5 shows phosphate oxygen at the topmost layer with calcium ions and protonated phosphate groups (P-O-H) embedded in the subsurface layer (Figure S12s). At pH 10, this plane has calcium ions on the topmost layer and phosphate oxygen in the sublayer. With surfaces equilibrated at both pH levels, the calcium ions are found to dissociate to varying extents. The C-P distances of $C_{\alpha \nu}$ C_{γ} and C_{CO} determined by MD simulation for both pH 5 and 10 show good agreement with the distances obtained from REDOR (models (a), (b), (d) and (e) in Table S12). The C_{β} -P distances deviated by $\sim \pm 0.3$ Å from the experimental result, as listed in Table S12. In our previous study, cHAP was found to have a surface with a significant amount of hydroxylation associated with calcium ions.²⁷ Therefore, the surface model at pH 10 (Figure S12b) probably aligns better with the actual surface of cHAP, as this model shows a higher number of calcium ions.²

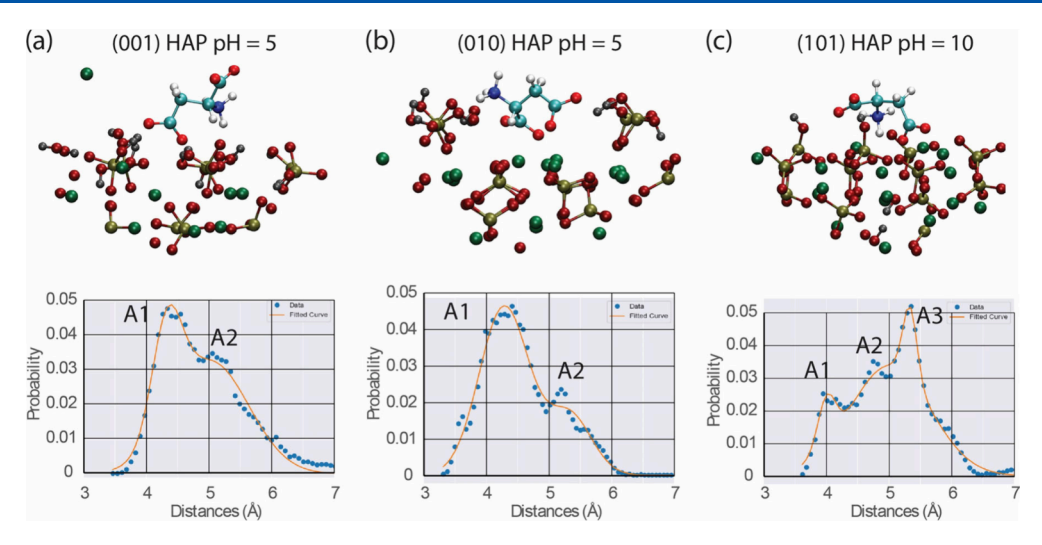


Figure 6. Selected adsorption geometries with high probability from MD simulations for Asp on (a) (001) HAP lattice plane at pH 5, (b) (010) or (100) HAP lattice plane at pH 5 and (c) (101) or (011) HAP lattice plane at pH 10. Color-coding: calcium in *green*, phosphorus in *gold*, and oxygen and hydrogen atoms on phosphate groups are in *maroon* and *gray*. For Asp molecules, nitrogen in *blue*, carbon in *cyan*, oxygen in *red* and hydrogen in *white*. The probability distributions of C_{β} -P distances (*blue dots*) and the fitted curves (*orange*) of these selected models are also presented.

aHAP has the (100) lattice plane preferentially synthesized under a pH level from 4 to 7, thus the MD simulation results of (010) lattice plane (which is equivalent to (100) plane aforementioned) at pH 5 is selected as a representative model for this sample. The adsorption isotherm of Asp on aHAP clearly shows multiple layers of adsorbed Asp, therefore, the C-P distances measured by REDOR may be affected by the excess Asp, resulting in distances averaged by the inversed third power that are significantly longer than those only from the bound layer (Table 2). The initial surface structure of (010) plane consists of arrays of phosphate groups along the c axis with the rows of calcium atoms reside in the "grooves" between these phosphates (Figure S12c,d). After equilibration, the phosphate groups on the topmost layer seem to adopt protons from hydration. This equilibrated model coincides with one important conclusion regarding aHAP in our previous study, which clearly indicates the presence of protonated phosphate groups.²⁷ The binding structure of Asp on this type of lattice plane generally shows Asp molecules embedded in between the phosphates, contacting the calcium ions via carboxyl groups as presented in Figure 6b.

rHAP is a polycrystalline nanorod synthesized in a basic environment (pH ~ 10) with surfaces composed of (010) and (101) lattice planes.²⁷ The distances calculated from the MD simulations of Asp adsorbed on the (101) plane of HAP at pH 10 match accurately with the REDOR results as shown in Table 2. The optimized Asp-HAP binding model at this pH is presented in Figure 6c. Among all three types of synthesized HAP NPs, this type of HAP shows the highest affinity to Asp, as evidenced by isotherm analysis and the tightest binding distances through REDOR. Although rHAP shares the (010) plane with aHAP, Asp shows a different adsorption behavior on each type of HAP. One potential explanation is that (101) is the plane that dominates the adsorption of Asp on rHAP, leading to these differences observed. The initial surface of (101) at pH 5 shows a structure terminated with phosphate groups and structural OH, which are dissociated or have undergone reactions during the process of equilibration (Figure S12e). At pH 10, the topmost layers of both initial

and equilibrated surfaces are composed of alternating phosphate groups and calcium ions (Figure S12f).

3.4. Additional MD Simulation Results on Calcium and Nitrogen. The interatomic distances between carbon from Asp and calcium ions on HAP surfaces (C–Ca) have been evaluated from the MD simulations as shown in Table S14. In previous studies simulating the adsorption behavior of amino acids on HAP surfaces, the carboxyl groups have been identified as the primary groups involved in binding interactions with calcium ions. $^{17,83-86}$ The C_{CO}/C_{γ} –Ca distances determined from the MD simulations are \sim 3 Å, which aligns with these findings, although in some specific structures they are not always clearly depicted in the structural models. Similar conclusions can be drawn from the SSNMR data, which also indicates the involvement of carboxyl groups in the binding interactions. Further studies of these interactions will be focused on calcium through 43 Ca SSNMR experiments, work that is ongoing in the lab.

Additional binding interactions can occur between the $\mathrm{NH_3}^+$ groups and phosphate oxygen on HAP surfaces by direct H bonding $^{83,87-90}$ or via bridging water molecules. 91 The N–P distances by MD simulation are ~ 3.7 Å as shown in Table 2. The line broadening shown in 15 N CP-MAS NMR indicates the possible participation of the $\mathrm{NH_3}^+$ groups in Asp adsorption (Figure 4). However, the results from 13 C CP-MAS NMR, 13 C/ 31 P REDOR and MD simulation clearly indicate that the Asp carboxyl group binding to calcium as the strongest interaction.

3.5. Discussion. Numerous previous studies have proposed a variety of energy minimized surface models for each HAP lattice plane. Some earlier systematic studies by Ugliengo et al. have modeled and optimized (001) and (010) lattice planes in aqueous environment by *ab initio* computations. ^{2,92,93} The model of (101) surface have been reported by Stott et al. ¹⁶ Recent works by Heinz and co-workers focused on quantifying the Ca/P ratio and the distributions of protonation state of surface phosphate groups under physiological pH levels to provide structures of HAP lattice planes under realistic pH conditions. ^{21,24} The (001) surface is typically characterized by a topmost layer with one calcium ion (Ca1) with coordination

sites that are not completely filled, along with three surrounding calcium ions (Ca2) in the sublayer each coordinating with three phosphate groups in a unit cell.^{2,94} Surface Ca–OH moieties and hydrogenated phosphate groups are formed by the dissociation of water molecules.^{17,95} These interfacial surface characteristics are supported by the results of our previous work using ¹H and ³¹P MAS SSNMR.²⁷ This surface is expected to show a strong affinity to the carboxyl groups and an Asp-HAP binding structure centered around the exposed Ca1. The binding structures provided by MD simulations in this work, however, do not completely align with this structure. Instead, these calcium ions seem to dissociate from the surface during Asp binding. This effect will be further evaluated in future studies.

In the case of (010) surface, there are three model surfaces terminated with phosphate, Ca or OH at different ratios. 85,94,96,97 In this work, a surface terminated with phosphate groups is adopted because this surface carries similar structural features to the actual aHAP NPs synthesized based on the SSNMR results in our previous study. The equilibrated surface of Figure S12c has the P-O-H groups and structural OH near the surface. The P-O-H groups have been identified by CP kinetic experiment and the exchange between OH and surface water molecules have been confirmed experimentally by a few previous SSNMR studies including from our own lab. 27,98,99

Since rHAP mainly consists of (010) plane with a small portion of (101) surface, ⁸⁰ Asp is expected to show a similar adsorption behavior to aHAP. However, rHAP is found to show the lowest adsorption capacity but highest affinity to Asp among all three types of HAP NPs. Since rHAP is synthesized in a strongly basic environment (reflux near boiling point at pH \sim 10), its structure and reactivity differ from those synthesized in acidic or neutral solutions. The (101) lattice plane may also play a major role in adsorption, leading to uniquely strong binding interactions with Asp.

4. CONCLUSIONS

The adsorption of Asp on HAP NPs with different surface structures and morphologies have been evaluated with Langmuir adsorption isotherms, a bevy of SSNMR methods and MD simulation. The structural configurations and binding geometries of Asp at HAP NP interfaces were analyzed in detail using SSNMR techniques complemented by MD simulations. The ¹³C-³¹P interatomic distances measured by REDOR are in good agreement with those estimated in MD simulations, and tighter binding determined by REDOR correlates with higher binding affinity observed in Langmuir isotherms. Both SSNMR and MD approaches suggest similar binding conformations of Asp molecules that have the carboxyl groups closest to the HAP surface preferentially bound to exposed calcium ions that exhibit some degree of dissociation in MD simulations. NMR relaxation was also pursued (Figure S5) that shows molecular dynamics on the surface are highly dependent on the NPs morphology where highly curved surfaces have more dynamic Asp molecules (see the Supporting Information). Overall, this combination of Langmuir adsorption isotherms, SSNMR structural and dynamic characterization and MD simulation have provided considerable new insights into the influence of HAP morphology on Asp binding, structure and dynamics on HAP surfaces.

ASSOCIATED CONTENT

Supporting Information

The Supporting Information is available free of charge at https://pubs.acs.org/doi/10.1021/acs.langmuir.4c02880.

³¹P NMR CSA pattern line fitting of aHAP (**Figure S1**); Preparation of crystalline OPLS and its crystal structure by ¹³C-³¹P REDOR (Figure S2 and Table S1); Parameters of six HAP surface systems utilized in the MD simulations (Table S2); Surface coverage and the adsorption isotherms of Asp at various initial concentrations onto synthesized HAP at 25 °C (Table S3, Figure S3 and S4); The deconvolution of ¹³C resonances of $C_{\alpha \nu}$ $C_{\beta \nu}$ and $C_{CO,\nu}$ from free and bound Asp (Table S4); REDOR of Asp-HAP compared to simulations with two-spin systems (Figure S5); ¹³C and 1 H T_{1} relaxation times of Asp adsorbed on the surfaces of rHAP, aHAP, cHAP, and free Asp in the amorphous and crystalline form (Table S5); Probability distributions of C-P Distances by MD Simulations (Figures S6-S11 and Tables S6-S11); Initial and equilibrated surface models of HAP planes (Figure S12); The binding configurations of Asp bound to different HAP lattice planes and the C-P distances by MD simulations (Tables S12 and S13); MD simulation results of C-Ca distances (Table S14) (PDF)

AUTHOR INFORMATION

Corresponding Author

Gregory P. Holland — Department of Chemistry and Biochemistry, San Diego State University, San Diego, California 92182-1030, United States; orcid.org/0000-0003-3062-3391; Email: gholland@sdsu.edu

Authors

Yuan Li — Department of Chemistry and Biochemistry, San Diego State University, San Diego, California 92182-1030, United States; ⊙ orcid.org/0009-0005-2594-4918 Christian D. Lorenz — Department of Engineering, King's College London, London WC2R 2LS, United Kingdom;

Complete contact information is available at: https://pubs.acs.org/10.1021/acs.langmuir.4c02880

orcid.org/0000-0003-1028-4804

Author Contributions

Conceptualization, Y.L. and G.P.H.; experimental, data analysis and writing, Y.L.; review and editing, G.P.H.; MD simulation, C.D.L.; supervision, G.P.H. All authors have given approval to the final version of the manuscript.

Notes

The authors declare no competing financial interest.

ACKNOWLEDGMENTS

This material is based upon work supported by National Science Foundation (NSF) Grant No. 2304833. The authors thank the technical support of Dr. Ingrid Niesman, Electron Microscope Facility, San Diego State University for TEM imaging, and Dr. David Onofrei, NMR Facility, San Diego State University for assistance with NMR data acquisition. The authors acknowledge the use of facilities and instrumentation supported by NSF through the UC San Diego Materials Research Science and Engineering Center (UCSD MRSEC), grant # DMR-2011924. The authors thank the e-Research

department at King's College London for support of us to use the CREATE High Performance Computing (HPC) resource. We are grateful to the UK Materials and Molecular Modelling Hub, which is partially funded by EPSRC (EP/T022213/1, EP/W032260/1 and EP/P020194/1), for providing access to the Young and ARCHER2 HPC resources.

REFERENCES

- (1) Cutini, M.; Corno, M.; Costa, D.; Ugliengo, P. How Does Collagen Adsorb on Hydroxyapatite? Insights From Ab Initio Simulations on a Polyproline Type II Model. *J. Phys. Chem. C* **2019**, *123*, 7540–7550.
- (2) Corno, M.; Busco, C.; Bolis, V.; Tosoni, S.; Ugliengo, P. Water Adsorption on the Stoichiometric (001) and (010) Surfaces of Hydroxyapatite: A Periodic B3LYP Study. *Langmuir* **2009**, *25*, 2188–2198.
- (3) Reyes-Gasga, J.; Martinez-Pineiro, E. L.; Bres, E. F. Crystallographic Structure of Human Tooth Enamel by Electron Microscopy and X-Ray Diffraction: Hexagonal or Monoclinic? *J. Microsc.* **2012**, 248, 102–109.
- (4) Meneghini, C.; Dalconi, M. C.; Nuzzo, S.; Mobilio, S.; Wenk, R. H. Rietveld Refinement on X-Ray Diffraction Patterns of Bioapatite in Human Fetal Bones. *Biophys. J.* **2003**, *84*, 2021–2029.
- (5) Landis, W. J. Mineral Characterization in Calcifying Tissues: Atomic, Molecular and Macromolecular Perspectives. *Connect. Tissue Res.* **1996**, *34*, 239–246.
- (6) Xin, R.; Leng, Y.; Wang, N. HRTEM Study of the Mineral Phases in Human Cortical Bone. *Adv. Eng. Mater.* **2010**, *12*, B552–B557.
- (7) Wang, Y.; Azais, T.; Robin, M.; Vallee, A.; Catania, C.; Legriel, P.; Pehau-Arnaudet, G.; Babonneau, F.; Giraud-Guille, M. M.; Nassif, N. The Predominant Role of Collagen in the Nucleation, Growth, Structure and Orientation of Bone Apatite. *Nat. Mater.* **2012**, *11*, 724–733.
- (8) Goldberg, M.; et al. Dental Mineralization. *Int. J. Dev. Biol.* **1995**, 39, 93–110.
- (9) Olszta, M. J.; Cheng, X.; Jee, S. S.; Kumar, R.; Kim, Y.-Y.; Kaufman, M. J.; Douglas, E. P.; Gower, L. B. Bone Structure and Formation: A New Perspective. *Mater. Sci. Eng. R.* **2007**, *58*, 77–116.
- (10) Goldberga, I.; Li, R.; Duer, M. J. Collagen Structure-Function Relationships from Solid-State NMR Spectroscopy. *Acc. Chem. Res.* **2018**, *51*, 1621–1629.
- (11) Petruska, J. A.; Hodge, A. J. A Subunit Model for the Tropocollagen Macromolecule. *Proc. Natl. Acad. Sci. U. S. A.* **1964**, *51*, 871–876
- (12) Hodge, A. J.; Schmitt, F. O. The Charge Profile of the Tropocollagen Macromolecule and the Packing Arrangement in Native-Type Collagen Fibrils. *Proc. Natl. Acad. Sci. U. S. A.* **1960**, *46*, 186–197.
- (13) Orgel, J. P.; Irving, T. C.; Miller, A.; Wess, T. J. Microfibrillar Structure of Type I Collagen *in situ. Proc. Natl. Acad. Sci. U. S. A.* **2006**, *103*, 9001–9005.
- (14) Chapman, J. A. The Staining Pattern of Collagen Fibrils. I. An Analysis of Electron Micrographs. *Connect. Tissue. Res.* **1974**, *2*, 137–150.
- (15) Mann, S. Biomineralization Principles and Concepts in Bioinorganic Materials Chemistry; Oxford, 2001.
- (16) Astala, R.; Stott, M. J. First-Principles Study of Hydroxyapatite Surfaces and Water Adsorption. *Phys. Rev. B* **2008**, *78*, 075427.
- (17) Zeglinski, J.; Nolan, M.; Thompson, D.; Tofail, S. A. M. Reassigning the Most Stable Surface of Hydroxyapatite to the Water Resistant Hydroxyl Terminated (010) Surface. *Surf. Sci.* **2014**, *623*, 55–63.
- (18) Wang, X.; Zhang, L.; Liu, Z.; Zeng, Q.; Jiang, G.; Yang, M. Probing the Surface Structure of Hydroxyapatite Through Its Interaction with Hydroxyl: A First-Principles Study. *RSC Adv.* **2018**, *8*, 3716–3722.

- (19) Diallo-Garcia, S.; Osman, M. B.; Krafft, J.-M.; Casale, S.; Thomas, C.; Kubo, J.; Costentin, G. Identification of Surface Basic Sites and Acid-Base Pairs of Hydroxyapatite. *J. Phys. Chem. C* **2014**, *118*, 12744–12757.
- (20) Ben Osman, M.; Diallo Garcia, S.; Krafft, J. M.; Methivier, C.; Blanchard, J.; Yoshioka, T.; Kubo, J.; Costentin, G. Control of Calcium Accessibility Over Hydroxyapatite by Post-precipitation Steps: Influence on the Catalytic Reactivity Toward Alcohols. *Phys. Chem. Chem. Phys.* **2016**, *18*, 27837–27847.
- (21) Lin, T. J.; Heinz, H. Accurate Force Field Parameters and pH Resolved Surface Models for Hydroxyapatite to Understand Structure, Mechanics, Hydration, and Biological Interfaces. *J. Phys. Chem. C* **2016**, 120, 4975–4992.
- (22) Kresak, M.; Moreno, E. C.; Zahradnik, R. T.; Hay, D. I. Adsorption of Amino Acids onto Hydroxyapatite. *J. Colloid Interface Sci.* 1977, 59, 283–292.
- (23) Tavafoghi, M.; Cerruti, M. The Role of Amino Acids in Hydroxyapatite Mineralization. *J. R. Soc. Interface* **2016**, *13* (123), 0462
- (24) Hoff, S. E.; Liu, J.; Heinz, H. Binding Mechanism and Binding Free energy of Amino Acids and Citrate to Hydroxyapatite Surfaces as a Function of Crystallographic Facet, pH, and Electrolytes. *J. Colloid Interface Sci.* **2022**, *605*, 685–700.
- (25) Zhu, P. X.; Masuda, Y.; Koumoto, K. Site-Selective Adhesion of Hydroxyapatite Microparticles on Charged Surfaces in a Supersaturated Solution. *J. Colloid Interface Sci.* **2001**, 243, 31–36.
- (26) Harding, I. S.; Rashid, N.; Hing, K. A. Surface Charge and the Effect of Excess Calcium Ions on the Hydroxyapatite Surface. *Biomater.* **2005**, *26*, 6818–6826.
- (27) Li, Y.; Deguzman, M. A.; Heise, J. E.; Holland, G. P. Synthesis and Structural Characterization of Morphologically Distinct Nanoscale Hydroxyapatites. *J. Phys. Chem. C* **2022**, *126*, 12790–12801.
- (28) He, G.; Dahl, T.; Veis, A.; George, A. Nucleation of apatite crystals in vitro by self-assembled dentin matrix protein 1. *Nat. Mater.* **2003**, *2*, 552–558.
- (29) Hauschka, P. V.; Reid, M. L. Timed appearance of a calcium-binding protein containing gamma-carboxyglutamic acid in developing chick bone. *Dev. Biol.* 1978, 65, 426–434.
- (30) Simon, P.; Gruner, D.; Worch, H.; Pompe, W.; Lichte, H.; El Khassawna, T.; Heiss, C.; Wenisch, S.; Kniep, R. First Evidence of Octacalcium Phosphate@Osteocalcin Nanocomplex as Skeletal Bone Component Directing Collagen Triple-helix Nanofibril Mineralization. Sci. Rep. 2018, 8, 13696.
- (31) Chen, Y.; Bal, B. S.; Gorski, J. P. Calcium and Collagen Binding Properties of Osteopontin, Bone Sialoprotein, and Bone Acidic Glycoprotein-75 from Bone. *J. Biol. Chem.* **1992**, *267*, 24871–24878.
- (32) Dickens, F. The Citric Acid Content of Animal Tissues, with Reference to its Occurrence in Bone and Tumour. *Biochem. J.* **1941**, 35, 1011–1023.
- (33) Hu, Y. Y.; Rawal, A.; Schmidt-Rohr, K. Strongly Bound Citrate Stabilizes the Apatite Nanocrystals in Bone. *Proc. Natl. Acad. Sci. U. S. A.* **2010**, *107*, 22425–22429.
- (34) Silver, F. H.; Landis, W. J. Deposition of Apatite in Mineralizing Vertebrate Extracellular Matrices: A Model of Possible Nucleation Sites on Type I Collagen. *Connect. Tissue Res.* **2011**, *52*, 242–254.
- (35) Linde, A.; Bhown, M.; Butler, W. T. Noncollagenous Proteins of Dentin. A Re-examination of Proteins from Rat Incisor Dentin Utilizing Techniques to Avoid Artifacts. *J. Biol. Chem.* **1980**, 255, 5931–5942.
- (36) Linde, A. Dentin Matrix Proteins: Composition and Possible Functions in Calcification. *Anat. Rec.* **1989**, 224, 154–166.
- (37) Raghunathan, V.; Gibson, J. M.; Goobes, G.; Popham, J. M.; Louie, E. A.; Stayton, P. S.; Drobny, G. P. Homonuclear and Heteronuclear NMR Studies of a statherin Fragment Bound to Hydroxyapatite Crystals. *J. Phys. Chem. B* **2006**, *110*, 9324–9332.
- (38) Gibson, J. M.; Popham, J. M.; Raghunathan, V.; Stayton, P. S.; Drobny, G. P. A Solid-State NMR Study of the Dynamics and Interactions of Phenylalanine Rings in a Statherin Fragment Bound to Hydroxyapatite Crystals. *J. Am. Chem. Soc.* **2006**, *128*, 5364–5370.

- (39) Goobes, G.; Stayton, P. S.; Drobny, G. P. Solid State NMR Studies of Molecular Recognition at Protein-Mineral Interfaces. *Prog. Nucl. Magn. Reson. Spectrosc.* **2007**, *50*, 71–85.
- (40) Ndao, M.; Ash, J. T.; Breen, N. F.; Goobes, G.; Stayton, P. S.; Drobny, G. P. A ¹³C{³¹P} REDOR NMR Investigation of the Role of Glutamic Acid Residues in Statherin- Hydroxyapatite Recognition. *Langmuir* **2009**, *25*, 12136–12143.
- (41) Greenwood, A. I.; Clay, M. C.; Rienstra, C. M. ³¹P-Dephased, ¹³C-Detected REDOR for NMR Crystallography at Natural Isotopic Abundance. *J. Magn. Reson.* **2017**, *278*, 8–17.
- (42) Mueller, K. T.; Jarvie, T. P.; Aurentz, D. J.; RobertS, B. W. The REDOR Transform: Direct Calculation of Internuclear Couplings from Dipolar-dephasing NMR Data. *Chem. Phys. Lett.* **1995**, 242, 535–542.
- (43) Lattao, C.; Cao, X.; Li, Y.; Mao, J.; Schmidt-Rohr, K.; Chappell, M. A.; Miller, L. F.; dela Cruz, A. L.; Pignatello, J. J. Sorption Selectivity in Natural Organic Matter Studied with Nitroxyl Paramagnetic Relaxation Probes. *Environ. Sci. Technol.* **2012**, *46*, 12814–12822.
- (44) Guo, C.; Holland, G. P. Investigating Lysine Adsorption on Fumed Silica Nanoparticles. *J. Phys. Chem. C* **2014**, *118*, 25792–25801.
- (45) Zheng, G.; Jin, W.; Fan, P.; Feng, X.; Bai, Y.; Tao, T.; Yu, L. A Novel Method for Detecting Amino Acids Derivatized with Phenyl Isothiocyanate by High-Performance Liquid Chromatography-Electrospray Ionization Mass Spectrometry. *Int. J. Mass Spectrom.* **2015**, 392, 1–6.
- (46) Osterberg, T.; Wadsten, T. Physical State of L-Histidine after Freeze-Drying and Long-Term Storage. *Eur. J. Pharm. Sci.* **1999**, *8*, 301–308.
- (47) Metz, G.; Wu, X. L.; Smith, S. O. Ramped-Amplitude Cross Polarization in Magic-Angle-Spinning NMR. *J. Magn. Reson., Ser. A* **1994**, *110*, 219–227.
- (48) Kolodziejski, W.; Klinowski, J. Kinetics of Cross-Polarization in Solid-State NMR: A Guide for Chemists. *Chem. Rev.* **2002**, *102*, 613–628.
- (49) Vinod Chandran, C.; Madhu, P. K.; Kurur, N. D.; Brauniger, T. Swept-Frequency Two-Pulse Phase Modulation (SWf-TPPM) Sequences with Linear Sweep Profile for Heteronuclear Decoupling in Solid-State NMR. *Magn. Reson. Chem.* **2008**, *46*, 943–947.
- (50) Thakur, R. S.; Kurur, N. D.; Madhu, P. K. Swept-Frequency Two-Pulse Phase Modulation for Heteronuclear Dipolar Decoupling in Solid-State NMR. *Chem. Phys. Lett.* **2006**, 426, 459–463.
- (51) Morcombe, C. R.; Zilm, K. W. Chemical Shift Referencing in MAS Solid State NMR. J. Magn. Reson. 2003, 162, 479–486.
- (52) Torchia, D. A. The Measurement of Proton-Enhanced Carbon-13 T_1 Values by a Method Which Suppresses Artifacts. *J. Magn. Reson.* 1978, 30, 613–616.
- (53) Freeman, R.; Hill, H. D. W. Fourier Transform Study of NMR Spin-Lattice Relaxation by "Progressive Saturation. *J. Chem. Phys.* **1971**, *54*, 3367–3377.
- (54) Cory, D. G.; Ritchey, W. M. Inversion Recovery Cross-Polarization NMR in Solid Semicrystalline Polymers. *Macromolecules* **1989**, 22, 1611–1615.
- (55) Canet, D.; Levy, G. C.; Peat, I. R. Time Saving in ¹³C Spin-Lattice Relaxation Measurements by Inversion-Recovery. *J. Magn. Reson.* **1975**, *18*, 199–204.
- (56) Vold, R. L.; Waugh, J. S.; Klein, M. P.; Phelps, D. E. Measurement of Spin Relaxation in Complex Systems. *J. Chem. Phys.* **1968**, *48*, 3831–3832.
- (57) Frye, J. S. Comparison of Inversion-Recovery Methods for Measuring Longitudinal Relaxation Rates. *Concepts. Magn. Reson.* **1989**, *1*, 27–33.
- (58) Struppe, J.; et al. Expanding the Horizons for Structural Analysis of Fully Protonated Protein Assemblies by NMR Spectroscopy at MAS Frequencies above 100 kHz. *Solid State Nucl. Magn. Reson.* **2017**, 87, 117–125.
- (59) Rienstra, C. M.; Tucker-Kellogg, L.; Jaroniec, C. P.; Hohwy, M.; Reif, B.; McMahon, M. T.; Tidor, B.; Lozano-Perez, T.; Griffin, R.

- G. De novo Determination of Peptide Structure with Solid-State Magic-Angle Spinning NMR Spectroscopy. *Proc. Natl. Acad. Sci. U. S. A.* **2002**, *99*, 10260–10265.
- (60) Gullion, T.; Schaefer, J. Rotational-Echo Double-Resonance NMR. J. Magn. Reson. 1989, 81, 196–200.
- (61) Hong, M.; Schmidt-Rohr, K. Magic-Angle-Spinning NMR Techniques for Measuring Long-Range Distances in Biological Macromolecules. *Acc. Chem. Res.* **2013**, *46*, 2154–2163.
- (62) Sinha, N.; Schmidt-Rohr, K.; Hong, M. Compensation for Pulse Imperfections in Rotational-Echo Double-Resonance NMR by Composite Pulses and EXORCYCLE. *J. Magn. Reson.* **2004**, *168*, 358–365.
- (63) Bak, M.; Rasmussen, J. T.; Nielsen, N. C. SIMPSON: A General Simulation Program for Solid-State NMR Spectroscopy. *J. Magn. Reson.* **2000**, *147*, 296–330.
- (64) Bak, M.; Nielsen, N. C. REPULSION, A Novel Approach to Efficient Powder Averaging in Solid-State NMR. *J. Magn. Reson.* **1997**, 125, 132–139.
- (65) van Meerten, S. G. J.; Franssen, W. M. J.; Kentgens, A. P. M. ssNake: A Cross-Platform Open-Source NMR Data Processing and Fitting Application. *J. Magn. Reson.* **2019**, *301*, 56–66.
- (66) Wei, Y.; Lee, D. K.; Ramamoorthy, A. Solid-State ¹³C NMR Chemical Shift Anisotropy Tensors of Polypeptides. *J. Am. Chem. Soc.* **2001**, *123*, 6118–6126.
- (67) Gu, Z.; McDermott, A. Chemical Shielding Anisotropy of Protonated and Deprotonated Carboxylates in Amino Acids. *J. Am. Chem. Soc.* **1993**, *115*, 4282–4285.
- (68) Jo, S.; Kim, T.; Iyer, V. G.; Im, W. CHARMM-GUI: A Web-Based Graphical User Interface for CHARMM. *J. Comput. Chem.* **2008**, 29, 1859–1865.
- (69) Choi, Y. K.; et al. CHARMM-GUI Nanomaterial Modeler for Modeling and Simulation of Nanomaterial Systems. *J. Chem. Theory Comput.* **2022**, *18*, 479–493.
- (70) Heinz, H.; Lin, T. J.; Mishra, R. K.; Emami, F. S. Thermodynamically Consistent Free Fields for the Assembly of Inorganic, Organic, and Biological Nanostructures: the INTERFACE Force Field. *Langmuir* **2013**, *29*, 1754–1765.
- (71) Huang, J.; Rauscher, S.; Nawrocki, G.; Ran, T.; Feig, M.; de Groot, B. L.; Grubmuller, H.; MacKerell, A. D., Jr CHARMM36m: An Improved Force Field for Folded and Intrinsically Disordered Proteins. *Nat. Methods* **2017**, *14*, 71–73.
- (72) Gowers, R. J.; et al. MDAnalysis: A Python Package for the Rapid Analysis of Molecular Dynamics Simulations. In *Conference: Proc. of the 15th Python in Science Conf. (SCIPY 2016), July 11 2016*; SciPy, 2019.
- (73) Michaud-Agrawal, N.; Denning, E. J.; Woolf, T. B.; Beckstein, O. MD Analysis: A Toolkit for the Analysis of Molecular Dynamics Simulations. *J. Comput. Chem.* **2011**, *32*, 2319–2327.
- (74) Moreno, E. C.; Kresak, M.; Hay, D. I. Adsorption of Molecules of Biological Interest onto Hydroxyapatite. *Calcif. Tissue Int.* **1984**, *36*, 48–59.
- (75) Chiou, C. T. Partition and Adsorption of Organic Contaminants in Environmental Systems; John Wiley & Sons, Inc., 2002.
- (76) Guo, X.; Wang, J. Comparison of Linearization Methods for Modeling the Langmuir Adsorption Isotherm. *J. Mol. Liq.* **2019**, 296, 111850.
- (77) Wang, Y.; Wilson, D.; Harbison, G. S. Solid-State NMR and the Crystallization of Aspartic and Glutamic Acids. *Cryst. Growth Des.* **2016**, *16*, 625–631.
- (78) Matlahov, I.; Iline-Vul, T.; Abayev, M.; Lee, E. M. Y.; Nadav-Tsubery, M.; Keinan-Adamsky, K.; Gray, J. J.; Goobes, G. Interfacial Mineral-Peptide Properties of a Mineral Binding Peptide from Osteonectin and Bone-Like Apatite. *Chem. Mater.* **2015**, 27, 5562–5569.
- (79) Shcherbakov, A. A.; Hong, M. Rapid Measurement of Long-Range Distances in Proteins by Multidimensional ¹³C-¹⁹F REDOR NMR under Fast Magic-Angle Spinning. *J. Biomol. NMR* **2018**, *71*, 31–43.

- (80) Ivanchenko, P.; Delgado-Lopez, J. M.; Iafisco, M.; Gomez-Morales, J.; Tampieri, A.; Martra, G.; Sakhno, Y. On the Surface Effects of Citrates on Nano-Apatites: Evidence of a Decreased Hydrophilicity. *Sci. Rep.* **2017**, *7*, 8901.
- (81) Kis, V. K.; Czigany, Z.; Dallos, Z.; Nagy, D.; Dodony, I. HRTEM Study of Individual Bone Apatite Nanocrystals Reveals Symmetry Reduction with Respect to P6(3)/m Apatite. *Mater. Sci. Eng. C Mater. Biol. Appl.* **2019**, *104*, 109966.
- (82) Kusunoki, M.; Sakoishi, Y.; Makino, T.; Tsunemine, T.; Fujita, N.; Okada, Y.; Okai, D.; Togo, H.; Hayami, T. Orientation Control for a-Axis or c-Axis Oriented Crystal Films of Hydroxyapatite, and a Possible Growth Mechanism Derived from X-Ray Diffraction. *Appl. Surf. Sci.* 2019, 484, 433–440.
- (83) Filgueiras, M. R. T.; Mkhonto, D.; de Leeuw, N. H. Computer Simulations of the Adsorption of Citric Acid at Hydroxyapatite Surfaces. *J. Cryst. Growth* **2006**, 294, 60–68.
- (84) Wang, Q.; Wang, M.; Lu, X.; Wang, K.; Fang, L.; Ren, F.; Lu, G. Effects of Atomic-Level Nano-Structured Hydroxyapatite on Adsorption of Bone Morphogenetic Protein-7 and its Derived Peptide by Computer Simulation. *Sci. Rep.* **2017**, *7*, 15152.
- (85) Zhang, Z.; Pan, H.; Tang, R. Molecular Dynamics Simulations of the Adsorption of Amino Acids on the Hydroxyapatite {100}-Water Interface. FMSC 2008, 2, 239–245.
- (86) Wang, W.; Xue, Z.; Wang, R.; Wang, X.; Xu, D. Molecular Dynamics Exploration of the Growth Mechanism of Hydroxyapatite Nanoparticles Regulated by Glutamic Acid. *J. Phys. Chem. B* **2021**, 125, 5078–5088.
- (87) Almora-Barrios, N.; Austen, K. F.; de Leeuw, N. H. Density Functional Theory Study of the Binding of Glycine, Proline, and Hydroxyproline to the Hydroxyapatite (0001) and (0110) Surfaces. *Langmuir* **2009**, 25, 5018–5025.
- (88) Canepa, P.; Chiatti, F.; Corno, M.; Sakhno, Y.; Martra, G.; Ugliengo, P. Affinity of Hydroxyapatite (001) and (010) Surfaces to Formic and Alendronic Acids: A Quantum-Mechanical and Infrared Study. *Phys. Chem. Chem. Phys.* **2011**, *13*, 1099–1111.
- (89) Chiatti, F.; Delle Piane, M.; Ugliengo, P.; Corno, M. Water at Hydroxyapatite Surfaces: the Effect of Coverage and Surface Termination as Investigated by All-Electron B3LYP-D* Simulations. *Theor. Chem. Acc.* **2016**, *135*, 54.
- (90) Rimola, A.; Aschi, M.; Orlando, R.; Ugliengo, P. Does Adsorption at Hydroxyapatite Surfaces Induce Peptide Folding? Insights from Large-Scale B3LYP Calculations. *J. Am. Chem. Soc.* **2012**, *134*, 10899–10910.
- (91) Dong, X.; Wang, Q.; Wu, T.; Pan, H. Understanding Adsorption-Desorption Dynamics of BMP-2 on Dydroxyapatite (001) Surface. *Biophys. J.* **2007**, 93, 750–759.
- (92) Corno, M.; Orlando, R.; Civalleri, B.; Ugliengo, P. Periodic B3LYP Study of Hydroxyapatite (001) Surface Modelled by Thin Layer Slabs. *Eur. J. Mineral.* **2007**, *19*, 757–767.
- (93) Corno, M.; Busco, C.; Civalleri, B.; Ugliengo, P. Periodic ab initio Study of Structural and Vbrational Features of Hexagonal Hydroxyapatite Ca₁₀(PO₄)₆(OH)₂. *Phys. Chem. Chem. Phys.* **2006**, 8, 2464–2472.
- (94) Zahn, D.; Hochrein, O. Computational Study of Interfaces Between Hydroxyapatite and Water. *Phys. Chem. Chem. Phys.* **2003**, *5*, 4004–4007.
- (95) de Leeuw, N. H. A Computer Modelling Study of the Uptake and Segregation of Fluoride Ions at the Hydrated Hydroxyapatite (0001) Surface: introducing a $Ca_{10}(PO_4)_6(OH)_2$ Potential Model. Phys. Chem. Phys. 2004, 6, 1860–1866.
- (96) Pan, H.; Tao, J.; Xu, X.; Tang, R. Adsorption Processes of Gly and Glu Amino Acids on Hydroxyapatite Surfaces at the Atomic Level. *Langmuir* **2007**, 23, 8972–8981.
- (97) Ma, X.; Ellis, D. E. Initial Stages of Hydration and Zn Substitution/Occupation on Hydroxyapatite (0001) Surfaces. *Biomaterials* **2008**, *29*, 257–265.
- (98) Klimavicius, V.; Marsalka, A.; Kizalaite, A.; Zarkov, A.; Kareiva, A.; Aidas, K.; Hirschinger, J.; Balevicius, V. Step-by-Step from Amorphous Phosphate to Nano-Structured Calcium Hydroxyapatite:

- Monitoring by Solid-State ¹H and ³¹P NMR and Spin Dynamics. *Phys. Chem. Chem. Phys.* **2022**, 24, 18952–18965.
- (99) Jager, C.; Welzel, T.; Meyer-Zaika, W.; Epple, M. A Solid-State NMR Investigation of the Structure of Nanocrystalline Hydroxyapatite. *Magn. Reson. Chem.* **2006**, *44*, 573–580.